Applied Surface Science 555 (2021) 149662

Contents lists available at ScienceDirect

Applied Surface Science

journal homepage: www.elsevier.com/locate/apsusc

Full Length Article

The nucleation, radial growth, and bonding of TiO_2 deposited via atomic layer deposition on single-walled carbon nanotubes

Carlos Guerra-Nuñez [a,1,*], Barbara Putz [a], Raluca Savu [b], Meng Li [c], Yucheng Zhang [d], Rolf Erni [d], Stanislav Mochkalev [b], Johann Michler [a], Hyung Gyu Park [c,2], Ivo Utke [a,*]

[a] Laboratory for Mechanics of Materials and Nanostructure, EMPA, Swiss Federal Laboratories for Materials Science and Technology, Feuerwerkerstrasse 39, CH-3602 Thun, Switzerland
[b] Centro de Componentes Semicondutores, Universidade Estadual de Campinas, R. Joao Pandia Calogeras, 90, 13083-870, Campinas, SP, Brazil
[c] ETH Zürich, Nanoscience for Energy Technology and Sustainability, Department of Mechanical and Process Engineering, Tannenstrasse 3, Zürich CH-8092, Switzerland
[d] Electron Microscopy Center, EMPA, Swiss Federal Laboratories for Materials Science and Technology, Überlandstrasse 129, CH-8600 Dübendorf, Switzerland

ARTICLE INFO

Keywords:
Atomic layer deposition
Carbon nanotubes
Raman spectroscopy
TiO2
In-situ ALD

ABSTRACT

The ability to determine the radial growth rate of atomic layer deposited (ALD) films on quasi-inert surfaces can enable precise control of decorative particle size or film closure for specific applications. The radial-growth-per-cycle (rGPC) is proposed in this work to quantify how thin films nucleate and grow from defect sites on carbon surfaces until film closure. The ALD of TiO_2 on non-functionalized singled-walled carbon nanotubes (SWCNTs) was monitored using in-situ Raman measurements, which collects signal of hundreds of SWCNTs during deposition. The gradual increase of the intensity ratio between the D- and G-band I_D/I_G from the sp^2-to-sp^3 hybridization reveals the progression in which TiO_2 nuclei grow from surface defects towards the pristine surface until nuclei coalescence. The radial overgrowth of TiO_2 along the inert surface is mainly bound by Van der Waals forces. Chemical bonding to the surface only occurred on average every ~12 nm, equivalent to only ~1% of the carbon atoms chemically bonded to the film. The in-situ Raman measurements determined a nuclei rGPC of ~0.19 ± 0.02 nm at temperatures lower than 120 °C, the point of film closure at the SWCNT circumference and axis, and a finite induced compressive stress of ~1 GPa to the nanotubes.

1. Introduction

Surface functionalization and thin film coating remain as one of the fundamental routes to preserve or improve the chemical and physical properties of the parent material or develop new functionalities [1]. In this regard, carbon nanostructures (i.e., carbon nanotubes (CNTs), graphene, etc.) can benefit greatly from partial or full surface coverage by decoration or complete coating of the surface with thin homogenous films in order to be integrated into a wide range of applications and devices [2–5]. For this, Atomic Layer Deposition (ALD) offers an unrivalled advantage to coat high aspect ratio nanostructures with a precise control of the film thickness by sequentially adding precursor molecules to the substrate in a self-limiting manner [6–9]. The nucleation of ALD thin films and subsequent homogenous growth depends on the adsorption of the precursor molecules on surface active sites (i.e., OH groups) to promote the ligand exchange reaction and eventual chemisorption of the precursor molecules. In contrast, the reduction or lack of active sites inhibits the homogeneous nucleation of the ALD film. For instance, it is well known that on chemically inert sp^2 carbon materials (CNTs, graphene), this nucleation process depends entirely on the preferential chemisorption at defective sites as well as the adsorption/desorption behavior of the precursor molecules on the pristine surface [10,11]. Thus, the growth of ALD films on such materials is strongly influenced by the defect density and the competition between adsorption and desorption of the gas precursor molecules. Most of the understanding we have about the growth of ALD films on these sp^2 carbon surfaces is limited to the variability of the defect density but not on the growth characteristics of the film on the inert CNT surface.

* Corresponding authors.
E-mail addresses: carlos.guerra-nunez@empa.ch (C. Guerra-Nuñez), ivo.utke@empa.ch (I. Utke).
[1] Present Address: Swiss Cluster AG, Feuerwerkerstrasse 39, CH-3602 Thun, Switzerland.
[2] Present Address: Center for Low-Dimensional Transport Physics, Department of Mechanical Engineering, Pohang University of Science and Technology (POSTECH), Cheongam-ro 77, 37673, Pohang, Gyeongbuk, Republic of Korea.

https://doi.org/10.1016/j.apsusc.2021.149662
Received 9 December 2019; Received in revised form 15 March 2021; Accepted 24 March 2021
Available online 28 March 2021
0169-4332/

In the case of graphene or CNTs, chemical pre-treatments (acid, plasma, etc.) are still to date the preferred methods to prepare the surface prior to the ALD coating deposition process, by significantly increasing the number of defects to promote a more uniform film growth. Nevertheless, it has also been shown that using plasma or acid treatments can lead to an uncontrolled damage of the carbon structure and affect their electronic properties [12,13]. Besides defect density, it was shown that the substrate temperature during the ALD process can influence the nucleation and growth behavior of a film (i.e. TiO_2, precursors: Titanium tetraisopropoxide and H_2O) on *non-functionalized* multi-walled CNTs (MWCNTs, [14–16]) and on single-layer graphene (SLG) [17].

As mentioned, there is a good evidence that ALD films nucleate at the defect sites of sp^2 carbon materials and eventually coalesce into a homogenous film [18–21]. However, we are still lacking the full understanding of the latter process. By understanding how ALD films grow on carbon surfaces and how fast, we can precisely control the surface coverage of the carbon surface for a specific functionality. Additionally, it can help us understand the growth process of ALD films on similar surfaces with a low density of active sites, such as on noble metals or surfaces with self-assembled monolayers as used in selective-area ALD. In order to study these nucleation and growth phenomena, we used vertically-aligned single-walled carbon nanotubes (SWCNTs) as a model substrate to monitor the sp^2 domains with *in-situ* Raman spectroscopy during ALD of TiO_2 from titanium tetraisopropoxide (TTIP) and water precursors. It has been demonstrated that the combination of these two techniques can be useful to identify surface species during the deposition of Al_2O_3 on Ag nanospheres [22].

Raman spectroscopy is one of the most important characterization tools to investigate the degree of functionalization in sp^2 carbon structures and stresses induced in the nanostructure. The resonant Raman frequencies, associated band shifts and intensity ratio changes in carbon materials are well-documented for functionalization [23–29], induced defects [30–36], gas adsorption [18–21], elastic and compressive strains [37–40], and oxidation and thermal treatments [41,42]. Each of these effects has a specific Raman signature; the most notable processes to consider are the following:

(i) *Chemisorption (surface functionalization)* to the carbon atoms through different treatments (i.e. acid treatments, oxidation, plasma, etc.) has a particular Raman signature on the carbon structures. There is a clear increase of the D-band intensity upon functionalization, which is attributed to the sp^2-to-sp^3 transition of carbon atoms where functional groups are attached [1,43–45]. The intensity ratio between the D- and G-band (I_D/I_G ratio) is then the current measure of covalent bonding and sp^3 hybridization [24–32].

(ii) *Physisorption* is a reversible process in which adsorbates weakly bond to the carbon surface by Van der Waals forces, and this adsorption has a small and reversible effect in the Raman signatures of the CNTs [18,21,46]. Coating of carbon nanostructures with metal oxides via ALD has shown variation of the I_D/I_G ratio and frequency shifts of the Raman bands with relation to the number of cycles or deposition temperatures [14,16,47–49].

(iii) *Induced tensile and compressive stresses* present a unique linear frequency downshift [37,38] and upshift [50–53] of the Raman bands, respectively. This is caused by elongation or shortening of the C═C bonds of the lattice. Nevertheless, the Raman bands return to their original position after removing the applied stress, if no failure was induced.

(iv) *Thermal treatments* on SWCNTs are known to downshift the Raman frequencies, the values reported are comprised between 0.010 $cm^{-1}/°C$ [54] and 0.025 $cm^{-1}/°C$ [55]. Only above 250 °C a slight reduction in the intensity of the D-band is observed on both double-walled CNT (DWCNT) and SWCNT. Above 450 °C, this reduction becomes considerably more pronounced [41,42].

(v) *Inducing defects* to carbon structures has been an approach to elucidate the nature of the Raman bands, particularly to determine the source of the D-band intensity and its extent by deliberately increasing the defect density [30,31,33,34]. The model developed by Lucchese [34] and Cançado [31] for SLG correlates the I_D/I_G ratio to the size and distance between induced defects on the carbon surface.

In order to perform a detailed investigation on the effect of progressively adding ALD precursor molecules onto SWCNTs, we performed all of our Raman measurements *in-situ* during the ALD of TiO_2 at different substrate temperatures. This comes with the advantage of monitoring the Raman bands of SWCNTs at every stage of the TiO_2 deposition process and probing the same location without breaking vacuum. To do so, we built a mobile-ALD system, including fabrication of a custom-made micro-ALD reactor, which fits under the Raman microscope, as illustrated in Fig. 1a.

2. Experimental

2.1. Synthesis of SWCNTs

A 30 nm thick alumina film was deposited on a Si wafer by electron beam evaporation at a deposition rate of 0.2 Å s^{-1} and a chamber pressure of ~$1–2 \times 10^{-6}$ mbar. By bombarding the as-deposited alumina with an Ar+ beam (Oxford Ionfab 300Plus) at 100 mA and 600 eV at an impingement angle of 20° for 1 min, we obtained ion-beam-treated alumina. On the prepared alumina support, 2 Å of Fe were deposited via electron beam evaporation. The CVD of the vertically aligned single-walled carbon nanotubes (SWCNTs) was carried out in a cold-wall vertical reactor (Black Magic). The sample stage was heated up to 700 °C at 200 °C/min and kept at this temperature for 60 s. During the annealing, 200-sccm Ar and 800-sccm H_2 were flown at 8 mbar of pressure. Following the annealing, the chamber was stabilized at 700 °C and 5-sccm of C_2H_2 were added into the gas flow for the SWCNT growth. The vertically aligned SWCNTs had a mean diameter of ~3.8 nm with a length of ~10 μm measured by scanning electron microscopy (SEM). Around 2/3 of the SWCNTs were identified to be semiconducting with a random chiral distribution. A full detail of the synthesis can be found in [56].

2.2. Deposition of ALD TiO_2

The mobile-ALD system consists of a manifold with a line of Ar gas controlled by a mass flow controller and two precursor inlets leading to the micro-reactor [57]. The SWCNT samples were loaded into the micro-reactor, which was mounted underneath the Raman microscope (see Fig. 1a). The reactor is covered with a 500 μm thick fused silica window (Markoptics) transparent to the wavelength of 532 nm. The same heating tape that heats the reactor was also wrapped around the edges of this window, so the temperature of the window is expected to be similar to the reactor. The depositions of TiO_2 on the SWCNTs were performed at a reactor temperature of 60 °C, 120 °C, and 220 °C. For TiO_2 we used Titanium tetraisopropoxide ($Ti(OCH(CH_3)_2)_4$ - TTIP, Aldrich 97%) heated to 90 °C and deionized H_2O kept at room temperature. The manifold and vapor delivery lines leading to the micro-reactor were heated to 100 °C to avoid condensation. One ALD cycle consisted of alternating pulses of TTIP and H_2O of 5 s followed by a 5 s exposure, then purging with Ar for 30 s. The pulsing times used ensured the complete coverage from top to bottom of the vertically aligned SWCNTs with TiO_2, as we have reported in a previous work [14], which were chosen conservatively compared to the calculated amount elsewhere [58]. The average growth per cycle on Si substrates was found to be ~0.055 nm at 60 °C, as reported to be the average growth rate of TTIP-H_2O [59].

For every ALD experiment, TiO_2 was also deposited on the inner side of the fused silica window of the micro-reactor. Due to the heating setup

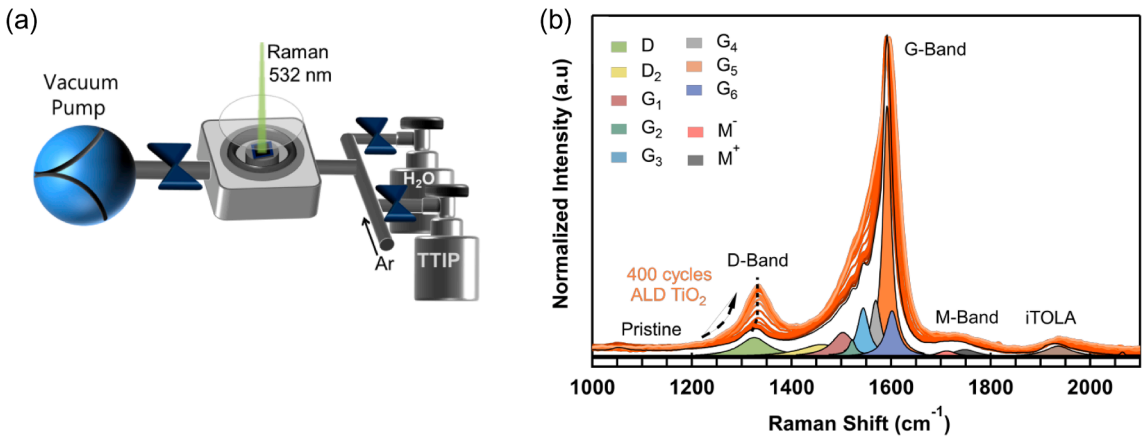

Fig. 1. (a) Schematic diagram of the micro-reactor placed under the Raman microscope covered with a fused silica window (~500 μm thick). There are two precursor bottles connected to the inlet and a vacuum pump connected to the outlet. (b) Normalized Raman spectra of the SWCNTs obtained during the deposition of TiO_2 at a substrate temperature of 60 °C and the corresponding Lorentzian peaks at 0 cycles (pristine) for the main Raman bands. Laser wavelength is 532 nm.

explained above, we expect the window temperature to be similar and we expect the same thickness of TiO_2 deposited on the samples to be deposited on that window. However, this thin TiO_2 layer on the window has no effect on the *in-situ* Raman measurements, detailed in the next paragraph, or their resolution. Due to the 3D structure and arrangement of the CNTs, the interaction volume of the TiO_2 coating for Raman spectroscopy is much larger as compared to the same coating in form of a single thin film (2–10 nm) on the silica window. For instance, it was therefore possible to measure and detect a 2 nm TiO_2 anatase coating on CNTs due to the large interaction volume, which would prove impossible in single thin film form. Furthermore, conclusions drawn within this manuscript are based on analysis of the carbon signal originating from CNTs and for every experiment a new silica window was installed.

Because of the very small size of the samples needed for the *in-situ* micro-reactor, we performed additional depositions on a home-made ALD reactor with similar parameters on SWCNT samples to use for X-ray photoelectron spectroscopy (XPS) measurements, SEM, and transmission electron microscopy (TEM) observation.

2.3. In-situ Raman spectroscopy during ALD

Confocal Raman spectroscopy was performed using an upright NT-MDT NTEGRA Raman microscope featuring a laser source with a wavelength of 532 nm and a 50× objective lens with a numerical aperture of 0.55. Spectra were recorded at a spectral resolution of ~2.5 cm^{-1} with a 30 s exposure. The use of a neutral density filter kept the laser power below 100 μW after the microscope objective in order to avoid inducing any side photochemistry or phase transformation of TiO_2. We found that increasing the laser intensity above 1 mW could locally induce phase transformation of amorphous into anatase TiO_2. The SWCNT samples were measured before and after vacuum, and at room temperature before increasing the substrate temperature. After equilibration of the substrate temperature and before deposition, a measurement was performed to be the reference (0 cycles) for every experiment. After that, we measured a Raman spectrum at the end of every ALD cycle for the first 5 cycles and then after every other 5 to 20 cycles. All measurements were performed in vacuum with an Ar flow of 10 sccm at the end of a cycle. The thermal shift of the peak positions for SWCNTs has been reported to be a downshift between 0.010 $cm^{-1}/°C$ and 0.030 $cm^{-1}/°C$ [54,55], which agrees well to our measurements performed at room temperature and after heating to a certain deposition temperature. Therefore, after the initial shift of the band positions at our substrate temperatures, we do not expect any subsequent shift during deposition caused by thermal shifts.

2.4. Additional characterization methods

The *ex-situ* XPS measurements were performed in a *Quantum2000* from Physical Electronics using a monochromatized Al Kα source (1486.6 eV). The X-ray spot had a diameter of 150 μm and operated at a power of 30 W at 15 kV. A neutralizer gun was used at 1.3 V and 20 μA. The core level spectra were fitted using a nonlinear least-squares line shape analysis after subtraction of a Shirley background. The spectra were aligned to the characteristic asymmetric peak of graphite structures at ~284 eV, and fitted with an asymmetric Doniach-Sunjic (DS) line-shape and a FWHM of 0.98–1.1 eV. The other C 1s components were fitted using a Gaussian-Lorentzian line-shape and setting the FWHM between ~0.9 and ~1.2 eV. SEM images of the cross-section were acquired using a high-resolution scanning electron microscope (SEM, Hitachi S4800, Japan) after cleaving the samples in half and analyzing the cross-section. Transmission electron microscopy (TEM) samples were prepared by dispersing the SWCNTs in methanol, ultrasonication for 5 min and pipetting a few droplets of the solution onto a lacey carbon film. TEM was conducted on a JEOL2200FX microscope operated at 200 kV. A short exposure time of typically 0.5 s was used in high-resolution TEM to avoid beam-induced damage or phase transformation.

3. Results

The main tangential modes of the SWCNTs are shown in Fig. 1b. These are characterized by the high energy modes (~1500–1600 cm^{-1}) or G-band which is the main Raman signature for all sp^2 carbon structures and originates from the graphitic in-plane sp^2 C-C stretching modes from tangential and longitudinal optical phonons (iTO and iLO). In SWCNTs, owing to its curvature, there are three higher frequency modes (HFM) and three lower frequency modes (LFM), labelled here as G_1- G_6 for practical purposes. The LFM, G_1 – G_3 are located at ~1500, ~1520, and ~1542 cm^{-1}, respectively, which stretch along the circumference of the nanotubes. The HFM, G_4- G_6 located at ~1567, ~1591 and ~1600 cm^{-1}, respectively, arise from the stretching modes along the carbon nanotube axis [26,60,61]. The main G-band considered in this work and other studies is the fitted G_5 band at 1591 cm^{-1}, referred to as only the G-band here. This peak is the one considered for the I_D/I_G calculations. The D-band is activated by the scattering of one iTO phonon and then inelastically scattered by a defect in the hexagonal lattice. The D-band at ~1324 cm^{-1} is thus assigned to the amount of disorder in the sp^2 lattice caused by defects, vacancies, and sp^3 atoms, etc. For this reason, the intensity ratio between the D- and G-band (I_D/I_G) is indicative of the quality of the nanotubes, and can qualitatively determine the sp^2-sp^3 transition states upon functionalization and the distance between these

sites [26,60]. The additional peak close to the D-band is labelled D_2 at ~1470 cm^{-1} and resembles that of amorphous carbon in MWCNTs [62]. In addition, SWCNTs present second-order and combination modes, which are less mentioned in literature, but still used here in the fitting procedure.

The M−bands, M^- and M^+, respectively, are overtone bands located at ~1710 and ~1745 cm^{-1} attributed to out-of-plane optical phonons. The peak at ~1950 cm^{-1} referred to as iTOLA, is a combination mode for the in-plane transverse optical (iTO) and longitudinal acoustic modes (LA) [63].

Once the SWCNTs samples were placed in the micro-reactor, they were measured before every deposition at their respective deposition temperature, which is the reference at 0 cycles. After that, we measured a Raman spectrum at the end of every cycle for the first 5 cycles and then after every other 5–20 cycles until reaching 400 cycles of sequential addition of TTIP and water. Fig. 1b then shows the spectra obtained during the deposition of 400 cycles of TiO_2 at a substrate temperature of 60 °C, and the corresponding fitted Lorentzian peaks of the pristine sample. From the spectra, one can already observe a shift and broadening of the G-bands and a clear increase in the intensity of the D-band, as well as the inner G-bands, all compared to the main G-band (G_5). In Figs. S1–S5 in the supporting information, we show how the frequency and FWHM upshifts during ALD until reaching a plateau at about 120 cycles. The final upshift of ~9 cm^{-1} of the D-band corresponds roughly to ~1 GPa of compressive stress [52,64–66]. The upshift of ~6 cm^{-1} of the G-band in SLG is due to hole doping and corresponds to an upshift of the Fermi level by ~0.2 eV [67,68].

3.1. The I_D/I_G ratios

As already observed from Fig. 1, during the deposition of TiO_2 the intensities of the D-band, as well as of the inner G-bands (shown in Fig. S6 in the supporting information), increase with the number of cycles. Fig. 2a compares the I_D/I_G ratio measured during the deposition of TiO_2 on SWCNTs at different substrate temperatures. The first thing to notice is the relatively smaller I_D/I_G ratios before deposition (0 cycles) at higher temperatures, which can be appreciated in the inset in Fig. 2a.

It has to be noted first that not all of the SWCNTs samples or even different areas within the same sample have the same I_D/I_G ratio. This is because naturally, not all the SWCNTs or bundles have exactly the same amount of defects. The small difference between the I_D/I_G ratios then translates to a small difference in the defect density of the pristine samples, which is independent of temperature. When the temperature was increased from room temperature (RT) to the respective temperature of the ALD process (60 °C, 120 °C, 220 °C), a small decrease of the I_D/I_G ratio was observed, by comparing measurements of the samples at RT to the first measurement after a stable temperature had been reached (Fig. 2a, 0 cycles). The measured decrease of the I_D/I_G ratio was 5×10^{-5} and 2×10^{-3} when heating from RT to 60 °C and to 220 °C, respectively, caused by a "healing" effect of the carbon surface [23,41,42,69]. It is reported that only after increasing the temperature above 450 °C the I_D/I_G ratio starts to decrease considerably by removing some of the amorphous material and defects [41,42].

Thereafter, during the first 5 to 10 cycles of pulsing TTIP and H_2O there is a further decrease of the I_D/I_G ratio. This is related to an additional "healing" effect which became more significant when the substrate temperature increased towards 220 °C, dropping down ~0.005 during the first 5 cycles (see inset in Fig. 2a). This may be similar to the ALD "self-cleaning" behavior (i.e. removing the oxide surface) during the first cycles on other substrates [70,71].

After this effect the I_D/I_G ratio remained relatively unchanged until it increased at about ~30 cycles onwards, indicating there is a gradual sp^2-to-sp^3 hybridization of the carbon atoms as the cycles progress. Then, the I_D/I_G ratios at 60 °C and 120 °C reached a *plateau* after ~150 cycles, whereas at 220 °C it did not reach a defined *plateau* during the 400 cycles of the experiment.

What this shows is that there is a progression in the hybridization of sp^2-to-sp^3 carbon atoms during deposition, which ultimately halts, due to film closure (i.e., there is no further interaction between gas precursor and substrate).

It is known that ALD films deposited from certain precursors can contain carbon impurities, which can change as a function of temperature (lower temperature = higher amount of carbon residues). As mentioned in the supplementary data, approximately <1 at.% of carbon is still inside the TiO_2 films deposited at 60 °C, and this amount decreases to a value below detection limits at deposition temperatures higher than 120 °C. However, the D and G bands during Raman spectroscopy arise stricly from the CNTs and therefore, these carbon residues do not affect the measured I_D/I_G ratios. This is because the signal comes from the continuous sp^2 domains (G-Band) and the disruption of these sp^2 domains form an sp^3 carbon (D-Band). The isolated unreacted carbon ligands from the TTIP precursor do not contribute to the I_D/I_G ratio presented in Fig. 2a. The Raman spectra of a sample of dried TTIP precursor residues, exhibiting no D or G bands, is included in the supplementary material (Fig. S18).

Another important point to consider is the relation between the I_D/I_G ratio and the ratio of the integrated areas A_D/A_G. It is often debated whether the area or the intensity ratio should be used for further analysis, since the Raman signal intensity depends on different hardware variables [33]. For this reason, we show in Fig. S7 in the supplementary information that the integrated area ratio A_D/A_G scales linearly with the I_D/I_G ratio, being the former ~2.5 times more the value of the intensity ratio throughout the deposition at different temperatures.

The plateaus reached by the I_D/I_G ratio correlate to the SWCNT surface coverage and film closure of the TiO_2, which we observed from SEM images. Fig. 2b–c show as an example the SEM images of SWCNTs

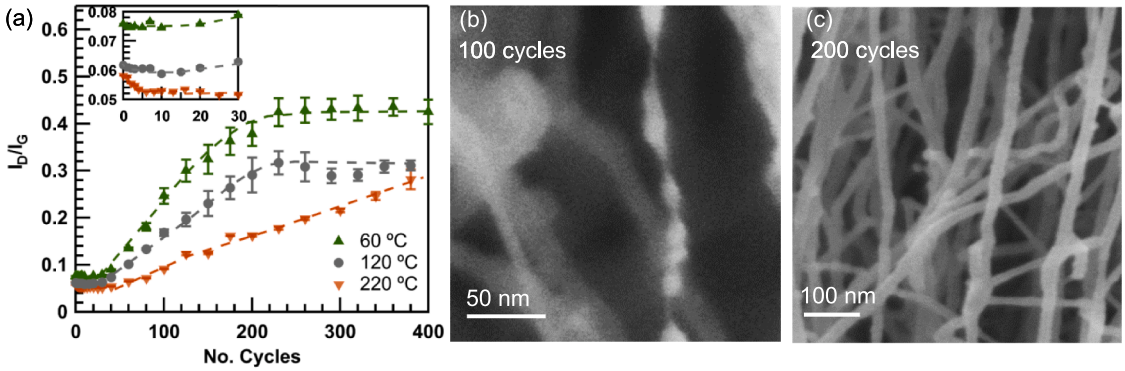

Fig. 2. (a) The difference in the intensity ratio between the D- and G-bands (I_D/I_G) of the SWCNTs coated with TiO_2 at different temperatures as a function of the number of cycles. SEM images of (b) 100 cycles and (c) 200 cycles of TiO_2 deposited at 60 °C.

coated with 100 and 200 cycles of TiO_2 at 60 °C. One can observe that at 100 cycles (Fig. 2b), the deposition of TiO_2 at 60 °C is not fully covering all the SWCNTs, as some nanotubes seem to display film closure and others are still not completely covered along the axis. Nevertheless, there is a majority of SWCNTs in which adjacent nuclei started to coalesce at the axis, which can be seen as grooves or "necked" film regions perpendicular to the nanotube axis (see Fig. S8 in the supporting information for more images). Likewise, one can also observe the isolated nuclei growing from different locations at the SWCNT circumference, which is the reason why from the 2D perspective from which these images were taken, the nuclei appear to have different thicknesses in each of the sides of the SWCNT.

As schematically illustrated in Fig. 3a, the nucleation centers (defects) on the SWCNTs are distributed in different locations along the nanotube circumference and axis. Once the TiO_2 film starts to grow from these nucleation centers, it will do so in the radial direction (2D) while still growing in volume (3D). Thus, the different apparent "thicknesses" of the nuclei is a matter of perspective of which side we are observing and from which point in the nanotube the nuclei started to grow. Any attempt to quantify a (3D) growth-per-cycle (GPC) from SEM images has to consider this situation. Fig. 2c then shows that at 200 cycles the TiO_2 film deposited at 60 °C (when the I_D/I_G ratio has already reached a plateau), appears to be fully coating the SWCNTs. Nevertheless, we still observed thickness gradients along the SWCNTs and a slight coarse morphology from the coalescence of neighboring nuclei (see Fig. S9 in the supporting information). Notwithstanding, it is remarkable which degree of homogeneity and SWCNT surface coverage can be achieved in such a pristine surface without any functionalization pre-treatment, using the specific TiO_2 precursors TTIP and H_2O. We observed a similar behavior for the deposition at 120 °C, although with a more evident coarser morphology (see Fig. S10 in the supporting information). The deposition at 220 °C displayed larger uncoated regions even with 200 cycles as compared to the lower deposition temperatures (see Figs. S11–12 in the supporting information). This agrees well with the fact that the I_D/I_G ratio did not reach a plateau as it did at the lower temperatures.

The rise of the I_D/I_G ratio with the number of cycles is directly related to the degree of functionalization of the SWCNTs, caused by the irreversible adsorption of TTIP molecules to the carbon surface and eventual chemisorption. Consequently, this results in the sp^2-to-sp^3 transition of some of the carbon atoms. This was further confirmed with ex-situ XPS measurements discussed in Figs. S13–S14 in the supporting information.

The progressive increase of the I_D/I_G ratio is thus directly related to the sp^3 formation, and one can determine the distance between point defects, or in this case, the distance between nucleation centers and the newly generated sp^3 sites as we keep adding TTIP and water molecules in an ALD fashion.

3.2. Quantifying the nucleation sites

As a starting point, we can assume the SWCNTs to be a rolled graphene sheet and thereby, the intensity ratios between the D- and G-bands and their nature are physically comparable to that of SLG. That being said, first consider the pristine SWCNTs with a random distribution of point defects, such as a C—H, C—OH, C—O—C, C═O, etc., with an average distance L_{n0} between them as depicted in Fig. 3a. As formulated by Lucchese et al. and Cançado et al., [31,34] the point defects with radius r_S will not contribute to the D-band's intensity, since the excited electrons from this point will be scattered outside of this area and mainly contribute to the G-band. On the other hand, in the region outside this point, termed the "activated" area with radius r_A, the excited electrons are close and live long enough to experience a scattering process by said defect, and will be mostly contributing to the D-band's intensity. The distance $r_A - r_S$ is then defined as the relaxation length in which the D-band is activated. This distance has been determined to keep the relation r_A-$r_S = 2$ nm [31,34].

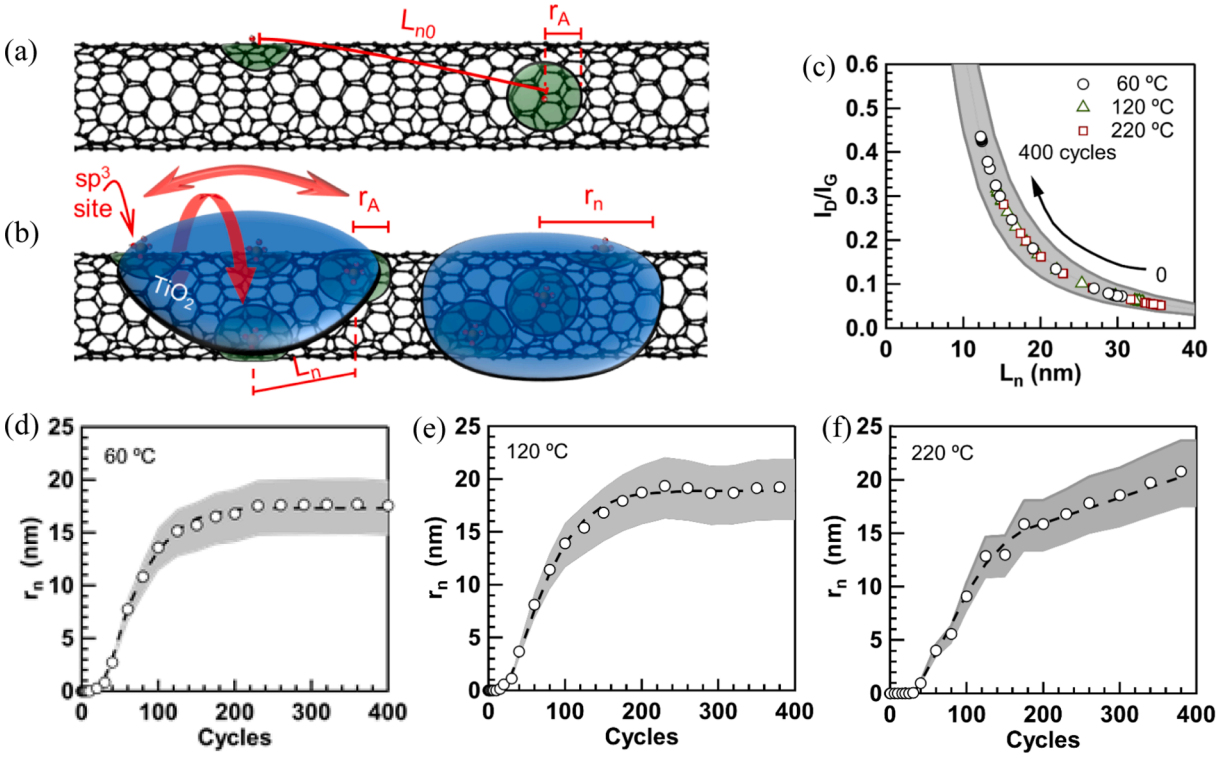

Fig. 3. (a) Schematic illustration of the horizontal projection of the distance L_{n0} between nucleation centers (not to scale). (b) Schematic illustration of the radial growth of the TiO_2 nuclei along the SWCNTs with a distance between nucleation centers, L_{n0}, and the distance between sp^3 sites, L_n, with radius $r_A = 2$ nm. (c) The distance between sp^3 sites L_n for every experimental I_D/I_G ratio measured during the deposition of TiO_2 on SWCNTs at different temperatures using Eq. (1). (d–f) The radius r_n of the TiO_2 nuclei as a function of the number of cycles at (d) 60 °C, (e) 120 °C, and (f) 220 °C. The shaded areas represent the boarders using $C_A = 5.4 \pm 1.6$.

Then, we considered the model derived by Cançado et al. to quantify the distance L_D between structural defects, namely holes breaking the lattice in SLG:[31]

$$\frac{I_D}{I_G} \approx C_A \cdot \frac{(r_A{}^2 - r_S{}^2)}{(r_A{}^2 - 2r_S{}^2)} \left[e^{-\left(\frac{\pi r_S{}^2}{L_D{}^2}\right)} - e^{-\left(\frac{\pi (r_A{}^2 - r_S{}^2)}{L_D{}^2}\right)} \right] \quad (1)$$

where C_A corresponds to the maximum I_D/I_G ratio in the hypothetical event in which the D–band is activated across the sample without losing the hexagonal structure and reported to depend on the laser's energy by $\sim(160 \pm 48)/eV^{\wedge 4}$ or $C_A = 5.4 \pm 1.6$ for a wavelength of 532 nm [31]. The parameters r_S and r_A correspond to the structural radius of a defect and the radius of the area activated by this defect, respectively, as defined previously [34].

To adapt this model to our scenario we considered the radius of any single sp^3 site to be $r_S = 0$ and therefore $r_A \approx 2$. In the case study of ion induced holes in SLG from Lucchese and Cançado [31,34], r_S is intended for the radius of a structural defect breaking the lattice (see Fig. S15a in the supporting information). In that case, the defective carbons at the perimeter of the hole contribute to the D-band's intensity through the activated area, whereas in our case, hybridized sp^3 carbons do not break the lattice. Even though a single sp^3 carbon atom itself does not contribute to the D-band, the activated area around it does. Then, by fixing $r_S = 0$ and $r_A = 2$ nm we can rewrite Eq. (1) in terms of the distance between defects, or in our case, nucleation sites, *Ln*:

$$\frac{I_D}{I_G} \approx C_A \cdot \left[1 - e^{-\left(\frac{4 \cdot \pi}{L_n{}^2}\right)} \right] \quad (2)$$

This means that we are considering that no sp^3 hybridized carbon atom breaks the hexagonal ring. It has been reported that even during oxygen plasma treatment on SLG, first there is a generation of partially oxidized carbons, which are mainly sp^3 without breaking the graphene lattice, see Zandiatashbar et al. [36] for details. In our case, we assume that the eventual chemisorption of a TTIP molecule with a carbon atom proceeds similarly without breaking the lattice. By choosing $r_S = 0$ then, in the hypothetical scenario in which new hybridized sp^3 carbon atoms increase in number until covering the whole surface, consequently reducing the distance L_n between them to the C-C bond length (0.142 nm), then the I_D/I_G ratio reaches the maximum possible. This occurs when the D-band is fully activated and hence the I_D/I_G ratio reaches the value of $C_A = 5.4 \pm 1.6$ (see Figs. S15–16 in the supporting information for further discussion).

First, we quantified the distance between the initial nucleation centers L_{n0}, (before coating) using Eq. (2) and the experimental I_D/I_G ratio of the pristine SWCNTs measured at 60, 120 and 220 °C. The average distance between nucleation centers on the pristine SWCNTs at 60 °C was about ~30 ± 5 nm in average, which is comparable to the defect density reported for SLG [35,72]. As discussed previously, we observed that for the SWCNTs measured before deposition at 120 and 220 °C, the I_D/I_G ratio is slightly lower and during the first 5 cycles the small decrease in the ratio caused this distance to increase to ~34 ± 5 nm, and ~36 ± 5 nm, respectively. This is to be expected if some of the defect sites are removed from the walls ("self-cleaning") at higher temperatures.

The concept of self-cleaning processes of CNTs and other surfaces at elevated temperatures and during ALD deposition is well established in literature [23,41,42,69]. For CNTs, the proposed mechanisms during annealing induced self-cleaning include thermally activated removal of defects and amorphous material [41,42], inducing mild changes in the carbon surface chemistry that shift the Raman reading. On other substrates, removal of the oxide surface during the first few cycles of ALD has been identified as a cleaning mechanism [70,71]. Strictly speaking, the cleaning process envisaged in this work comprises both of these components: (i) thermally activated self-cleaning, as previously proposed and notably/significantly observed for CNTs above 250 °C/450 °C, respectively [41,42], and (ii) cleaning assisted by ALD precursor molecules. The first effect is visible in a very small reduction of the ID/IG ratio after heating from room temperature to the respective ALD temperatures, as described earlier. The second effect takes place during the initial stages of ALD deposition and manifests itself as a decrease in the ID/IG ratio during the first few ALD cycles. While this is mainly attributed to cleaning induced by ALD precursor molecules, it is impossible to unambiguously separate and exclude potential contribution from pure thermal annealing at this point, because of the elevated temperature during ALD deposition. Certainly, precursor assisted cleaning is temperature dependent, as the observed decrease in ID/IG during the first 5–10 ALD cycles becomes more pronounced with increasing temperature (inset Fig. 2a).

Fig. S15b shows that for I_D/I_G ratios below 0.1, a small difference in the I_D/I_G ratio has a significant effect in the distance between nucleation centers, L_n. We also keep in mind that this average entails a combination of smaller and larger distances between nucleation centers within a SWCNT. These nucleation centers are fixed in the sidewalls, and the nucleation of TiO_2 then starts from these centers with the chemisorption of a TTIP molecule. As we continue sequentially adding TTIP and water molecules, the TiO_2 nuclei grow radially from these centers. Consequently, this generates a certain amount of "new" sp^3 sites as the nuclei grow, as illustrated in Fig. 3b. The creation of sp^3 sites for example solely by pulsing water has been previously observed through experiments and modelling. Vecera et al. [24,25] have shown by Raman measurements and DFT calculations that the amount of these defects is very small, approximately 0.1% of sp^3 sites. Similarly, the amount of new sp^3 sites generated by the growing TiO_2 nuclei is equally low.

Thereafter, we quantified the average distance between the "new" (and existing) sp^3 sites as the number of cycles increases. Fig. 3c shows how the experimental I_D/I_G obtained from the *in-situ* Raman measurements during deposition of TiO_2 at different temperatures translates into L_n using Eq. (2). Every I_D/I_G measured corresponds to a specific L_n. The grey area in the following plots represents the boarders using $C_A = 5.4 \pm 1.6$.

The evolution of the I_D/I_G ratio with the number of cycles and the resulting L_n, show that the deposition of TiO_2 onto SWCNTs entails a progression of increasing the nuclei size radially along the SWCNTs from the nucleation centers, as the average distance between them and the "new" sp^3 sites is gradually reduced as the number of cycles increases. The average distance reached between them after the I_D/I_G *plateaus* is L_n ~ 12 ± 2 nm, 14 ± 2 nm, and 15 ± 2 nm at a deposition temperature of 60, 120 and 220 °C, respectively.

The small I_D/I_G ratios of <0.4 obtained after coating and the corresponding average lateral distance between sp^3 bonds of ~12 nm constitute only 1.2 ± 0.2% of SWCNT functionalization ($L_n \approx 0.142$ nm is the 100%). In other words, as the nuclei grow, only a very small percentage of the carbon atoms are hybridized into sp^3 and hold the TiO_2 film by a chemical bond, the rest ~99% of the coalesced film is bound by van der Waals forces. The ~1% of chemical bonds between the TiO_2 coating and the carbon surface correspond to an average linear distance between sp^3 bonds of ~12 nm, i.e. ~60–80 carbon atoms in a straight line, or about 7 bonds per 1000 nm^2, or about 1 bond per ~916 C-hexagons. This average distance involves that within the growing nuclei the distance between "newly" generated sp^3 sites and the initial nucleation center L_{n0} is shorter, as one can observe from the progression of Ln with the number of cycles, but the initial separation between nucleation centers of ~30 nm and larger modifies this average. This is the reason why the I_D/I_G ratio remains almost unchanged for the first ~20 cycles; it is only when the average distance Ln starts to become shorter that there is a visible increase of the ratio.

Nevertheless, the scarce but eventual incorporation of sp^3 sites with the number of cycles shows the gradual growth of the TiO_2 nuclei along the SWCNT surface until coalescence of the majority of the nuclei and

hence, film closure occurs. We show in Fig. 3d–f the average radius of the TiO_2 nuclei from the relation $r_n = L_{n0} - L_n$, as a function of the number of cycles for every deposition temperature. We use L_{n0} to be the baseline of the average distance to be subtracted, because these initial sites are fixed in the carbon nanotubes, and will maintain this distance throughout the whole deposition process. One can observe that for the depositions at 60 and 120 °C, the radius of the nuclei plateaus (i.e., the nuclei stopped growing) at roughly half the distance of the initial separation between nucleation centers. At 60 °C, the nuclei stopped growing when they reached ~17 nm in average size and at 120 °C when they reached ~19 nm. This is about half of the distance of the (fixed) initial separation between the nucleation centers of ~30 ± 5 nm and ~34 ± 5 nm at 60 and 120 °C, respectively, and is the point where most of the SWCNTs reached film closure at the nanotube's axis. At 220 °C, the radius of the nuclei does not quite reach this half distance at the end of 400 cycles. The r_n at 220 °C reached larger values at the end of 400 cycles, due to the larger distance between the initial nucleation centers of L_{n0} ~ 36 ± 5 nm.

In Fig. S17 in the supporting information we show the histograms of the radius of the nuclei we measured from the SWCNTs after 100 cycles of TiO_2 deposited at 60 and 220 °C (from the SEM images shown in Figs. S8–12), as well as for the SWCNT diameter. The measured nuclei radii correspond to those calculated in Fig. 3d–f.

3.3. Quantifying the radial growth rate of the TiO_2 film

Thereafter, we calculated the radial (2D) growth rate-per-cycle (rGPC) of the TiO_2 nuclei by deriving the r_n as a function of the number of cycles from Fig. 3d–f. The rGPC represents the rate in which the base of the nuclei grows radially in contact with the surface of the CNTs, which is what can be directly calculated from the Raman measurements. This is different to the width of the nuclei that may not be "wetting" the surface.

In Fig. 4, we show the rGPC obtained at every deposition temperature. The depositions at 60 °C and 120 °C present almost exactly the same trend, increasing to a maximum rGPC of ~0.19 ± 0.02 nm between 30 and 60 cycles and then decreasing towards zero due to film closure. For the deposition at 220 °C, the maximum rGPC (~0.15 ± 0.02 nm) is lower than those at the lower temperatures are, and does not reach zero due to a lack of film closure, but it reaches a constant value of rGPC ~ 0.03 nm/cycle after 200 cycles. The first thing to notice is that the rGPC is not constant throughout the number of cycles as it does for the known layer-by-layer growth of ALD, and at some point it reached larger values than the conventional 3D GPC of 0.055 nm/cycle. Let us analyze the meaning of these values.

Contrary to the known growth of ALD on hydroxylated surfaces, the ALD growth on inert surfaces differs drastically in the number of available active sites at every new cycle. In a conventional hydroxylated planar surface (i.e., silicon substrate), the number of active sites (i.e., OH groups) is relatively constant in every new cycle, and therefore the GPC is constant and is influenced directly by the steric hindrance landscape [9,73]. In a quasi-chemically inert surface, the nucleation and growth starts from just one active site, the defect (nucleation center). During the first cycles we have seen there is a "healing effect" in which some of these defects are removed or not all react with the incoming TTIP molecules, often referred to as a "nucleation delay", but is due to a "self-cleaning", as discussed in [70,71]. Consequently, at the starting point, the rGPC in average is close to zero during the first cycles. The surviving defects can react with only one ligand from a single TTIP molecule, which leads this adsorbate to become the center of the nuclei (see Fig. 5a). Upon hydrolysis after the water pulse, this single adsorbate can provide (ideally) 3 more OH groups in the next cycle, and so on in the subsequent cycles. However, we cannot know how many of these ligands can be hydrolyzed and how many remain adsorbed to the carbon surface. Thereafter, the succeeding TTIP molecules experience a "steric hindrance-free" surrounding, because there are just no molecules in the vicinity. As the cycles progress, the number of active sites at the growing perimeter at the base of the nuclei will increase. Therefore, due to the changing density of OH groups, the rGPC does not display a constant rGPC but increases during growth, and can reach larger values than the conventional 3D GPC due to the "steric hindrance-free" landscape. The rGPC reached a maximum of ~0.19 ± 0.02 nm/cycle, which is half of the size of a Ti – O molecule [74]. In a similar situation, the growth of Pt nanowires on the step edges of HOPG also presented a larger lateral GPC than the conventional GPC [75]. From the width of the nanopillars, they have measured a total width GPC of 1.3 Å/cycle (or rGPC ~ 0.065 nm/cycle), which is half the size of the Pt atomic radii [74].

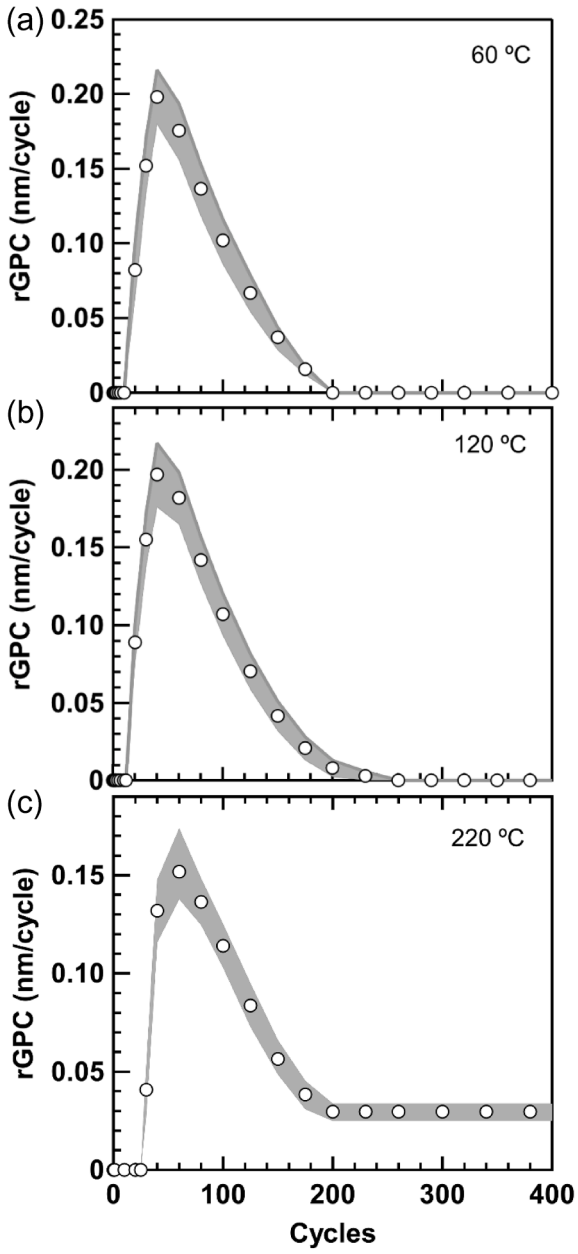

Fig. 4. The radial growth-per-cycle (rGPC) at (a) 60 °C, (b) 120 °C, and (a) 220 °C.

After this point, the rGPC starts to decrease from ~60 cycles onwards, which is the point when the nuclei reached a radius of ~6 nm (see Fig. 3d) and have coalesced with themselves at the opposite side of the circumference of the nanotube, as illustrated by the outer circle in red in Fig. 5a. The SWCNTs have an average of ~12 nm in circumference for a diameter of ~3.8 nm (see Fig. s17a in the supporting information).

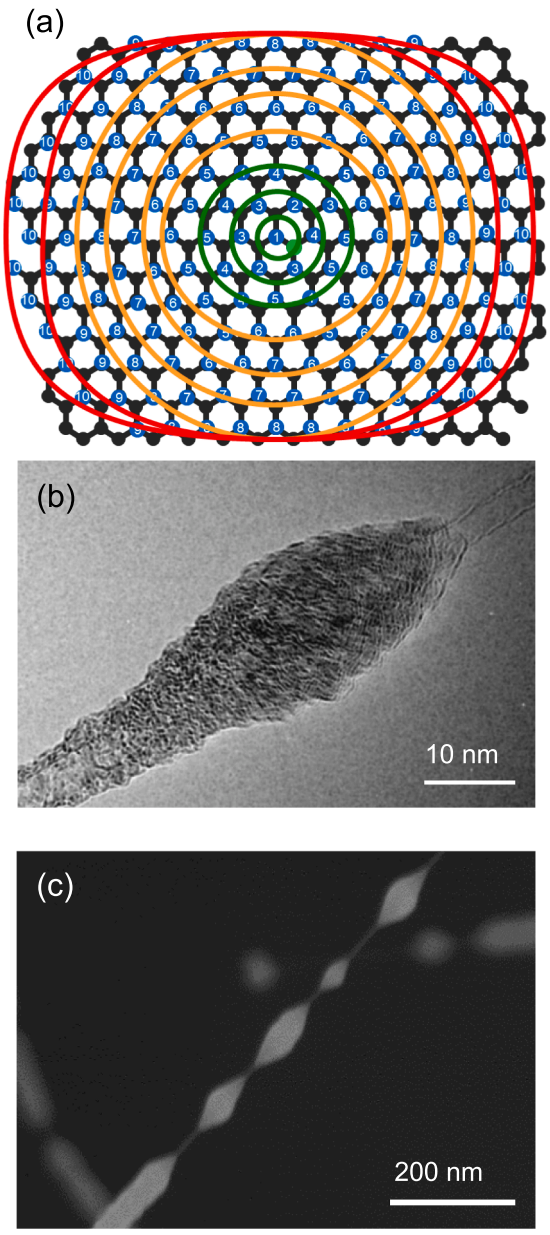

Fig. 5. (a) Schematic diagram of the growth behavior of TiO_2 on SWCNTs visualized as an unrolled graphene sheet starting from a nucleation center (green point) and growing radially. The circumference of the CNT is from top to bottom. As the nucleus grows radially, the circumference of the SWCNTs is coated first and then proceeds to grow axially along the nanotube while simultaneously growing in 3D. (b) TEM image of a SWCNT coated with 180 cycles of TiO_2 at 60 °C. (c) SEM image of a SWCNT coated with 600 cycles of TiO_2 at 60 °C. (For interpretation of the references to colour in this figure legend, the reader is referred to the web version of this article.)

The nuclei grow radially from a nucleation site and coalesce with themselves at the opposite side of the circumference of the nanotube when they reach ~6 nm, after which the perimeter of the nuclei decreases as they grow towards both ends at the nanotube axis. The reduction of the nuclei perimeter size and consequently the density of OH groups decrease the rGPC. The rGPC continues to decrease towards zero as some of the nuclei coalesce with neighboring nuclei at the axis of the CNTs while some others still continue to grow until reaching zero, which is when film closure occurs and the surface of the CNTs is covered. The rGPC at a specific number of cycles represents the average of what is happening in these scenarios, the Raman measurements take into account hundreds of CNTs and sp^3 sites.

On the other hand, at 220 °C, the "healing effect" during the first cycles is stronger and is seen as a longer "nucleation delay". The maximum rGPC (~0.15 ± 0.02 nm) is reached until 80 cycles, which is also, when the nuclei reached ~6 nm (see Fig. 3f) and coalesced with themselves, after which it starts to decrease. This rGPC is lower than at lower temperatures, most likely due to a weaker adsorption to the carbon surface and preferential chemisorption to the nuclei itself. At 40 cycles, the average rGPC of ~0.04 nm/cycle is close to that of the 3D GPC of TiO_2, which means the width of the nuclei grew as fast as the height, leading the nuclei to have a more spherical shape. This explains the spherical shape of the TiO_2 nuclei we have observed at this deposition temperature compared to the flat morphology of the nuclei deposited at lower temperatures, observed here on SWCNTs and on MWCNTs for only 20 cycles [14].

After 200 cycles, the rGPC reaches a constant value of about ~0.03 nm. This constant rGPC occurs when the perimeter on both sides of the nuclei is that of the SWCNT circumference without having coalesced with neighboring nuclei, as illustrated in Fig. 5a. At lower temperatures, this happens at 100 cycles when the rGPC is about ~0.11 ± 0.01 nm.

As ALD entails a sequential growth upon the presence of surface functional groups then, as soon as there are hydroxyl groups at the surface provided by the growing number of hydrolyzed TTIP adsorbates, the film grows vertically while it grows radially along the SWCNTs (3D growth). This GPC proceeds as it would with TTIP reacting with Ti-OH adsorbates (0.055 nm/cycle). Therefore, a nucleus exhibits a conical growth shape, having the thickest region at the initial nucleation site where the nucleation started.

In Fig. 5a, we schematically illustrate the radial growth on an unrolled SWCNT by sequentially adding TTIP molecules around a nucleation center, and how the nucleus simultaneously grows in 3D from the nucleation center towards both ends of the nanotube axis. The numbers represent the order in which a nucleus can grow depending on the possible available sites that start from the center, but are not related to the number of cycles. In the case when it is possible to find a region on the SWCNTs that the nucleation centers are further apart so that there is no coalescence between neighboring nuclei during growth, one can observe clearly this type of morphology.

In Fig. 5b, we show the TEM image of an isolated TiO_2 nucleus without apparent coalescence with other nuclei, which shows this type of morphology. The SWCNT with ~3.3 nm in diameter is coated with 180 cycles of TiO_2 at 60 °C. The TiO_2 nucleus extends up to ~44 ± 1.7 nm in length along the SWCNT.

The SWCNT seems to be in a parallel position with respect to the point of view of the image (i.e., the shape of the nucleus is symmetrical). Since there is no coalescence with other nuclei, we are considering then that at ~100 cycles the nucleus already coalesced with itself at the circumference, reaching an r_n of 13.3 ± 1.8 nm (see Fig. 3d).

At this point, the perimeter of the growing nucleus is constant (as depicted with the red triangle in Fig. 5a), and at this point we can consider the steady rGPC of ~0.1 ± 0.01 nm obtained at 100 cycles (see Fig. 4a). At this rGPC for the remaining 80 cycles adds to a total r_n of 21.5 ± 2.6 nm at the end of the 180 cycles, which is very close to the radius we have measured in the TEM image. Likewise, the SEM image in Fig. 5c shows a SWCNT coated with TiO_2 at 60 °C for 600 cycles. A portion of the SWCNT present a continuous coating when the neighboring nucleation centers are closer with each other and coalesced during growth, but still a groove from this merging can be observed at the middle of the image. However, in the case that nucleation centers are far apart, large areas of the SWCNTs can remain uncoated even after 600 cycles. Some nucleation centers seem to be even ~100–200 nm apart. The two individual nuclei at both ends of the SWCNT extend up to ~144 ± 4 nm in length along the SWCNT (~72 nm in radius). Applying the same criteria, in which the nuclei reach an r_n of 13.3 ± 1.8 nm at 100 cycles coalescing with themselves but without coalescing with neighboring nuclei, then the remaining ~58 nm for the rest 500 cycles

correspond to an rGPC of 0.11 ± 0.01 nm, which agrees well with those calculated previously. There is a smaller nucleus of ~85 ± 4 nm in length, but we suspect that a nucleation center may have been created during the 600 cycles of deposition and therefore presents a shorter length along the SWCNT.

3.4. Nucleation and growth mechanism

The deposition temperature contributes in two ways: first, the temperature inevitably modifies the surface chemistry; for higher temperatures (i.e., >120 °C) some of the defects or functional groups at the surface are removed ("self-cleaning"), resulting in a slight increase in the average distance between nucleation centers. The decrease in the I_D/I_G ratio when this distance is >20 nm is so small (within 0.005) that it is often overlooked. However, a small decrease of the I_D/I_G ratio could mean a drastic increase in the average distance between nucleation centers. The TTIP molecules (surface) diffuse until adsorbing to a nucleation center (defect) and eventually chemisorbing. As it appears, during the first 10–20 cycles, not all of these sites may be consumed, and at higher temperatures, some of these sites are even removed. The initial TTIP molecules that chemisorbed to these sites, after hydrolysis, serve as the starting point for subsequent TTIP molecules to attach with and thus become the center of the nuclei. As the number of cycles increases, the TTIP molecules chemisorb with the Ti-OHx adsorbates at the perimeter of the growing TiO_2 nuclei, while physisorbing to the carbon surface. This consequently provides a growing number of hydrolyzed adsorbate sites at the perimeter for the incoming TTIP. The rate, at which the nuclei grow radially, the rGPC, reached a maximum of ~0.19 ± 0.02 nm at low temperatures, which is about half of the Ti-O molecular size. This maximum rGPC was reached at about 40–60 cycles (see Fig. 4a–b), which coincides with the maximum possible perimeter size of the nuclei, just before coalescence with themselves at the opposite side of the SWCNT circumference, after which the nuclei perimeter decreases and consequently the rGPC.

Secondly, the temperature influences the adsorption of the gas molecules to the carbon surface. At higher temperatures the adsorption to the carbon surface is weaker and vertical growth is preferred rather than laterally (radially) and thus a lower rGPC, which explains the more spherical shape of the TiO_2 nuclei deposited at 220 °C.

The radial (2D) growth of TiO_2 is bound by van der Waals forces and therefore, the carbon surface retains the majority of its sp^2 nature. The relatively small increase of the I_D/I_G ratios and corresponding distance between sp^3 sites after coating show only ~1% of functionalized carbons (from an initial ~0.5%). The surface coverage of the carbon surface then depends on: i) the initial separation between the nucleation centers and ii) the rGPC of the metal oxide (i.e., dependent on temperature). When the distance between nucleation centers are far apart, the nuclei will coalesce at larger number of cycles. When the distance between nucleation centers is shorter than those presented here for pristine SWCNTs, the nuclei can coalesce at a shorter number of cycles and thus films appear to be more homogenous and continuous as demonstrated to be in *non-functionalized* MWCNTs [14,16]. For a rGPC close to the conventional 3D GPC then, nanopillars can be fabricated [75].

The precise knowledge of the radial growth rate of different materials on sp^2 carbon surfaces allows controlling the coating for decoration or full surface coverage for a specific application. The *in-situ* Raman-ALD system was essential to study this process and may therefore be useful to study different precursor chemistries and substrate materials. This may be particular interesting for any quasi-inert surface such as with self-assembled monolayers for selective ALD.

4. Conclusions

In this work, we have investigated how atomic layer deposited thin films (TiO_2) nucleate and radially grow on inert surfaces (SWCNTs). The *in-situ* Raman spectroscopy during the ALD of TiO_2 on SWNCTs at different temperatures was essential to characterize the same region of hundreds of carbon nanotubes at every stage of the deposition without breaking vacuum. The frequency shifts of the D- band suggest a gradual increase of induced compressive stress up to ~1 GPa during the growth of the TiO_2 nuclei, which starts to plateau after the nuclei have surrounded the SWCNT circumference. The frequency shifts of the G- bands corresponded to hole doping of the SWCNT. Both bands gradually increased with the number of ALD cycles and reached a plateau once the TiO_2 film closed at the surface, meaning that these effects are purely at the TiO_2-SWCNT interface, and do not continue after depositing more TiO_2 material. The I_D/I_G ratio presented a progressive increase with the number of ALD cycles, also reaching a plateau once TiO_2 film closure occurred. We then adapted the model developed by Lucchese and Cançado to translate the I_D/I_G ratio to the distance between sp^3 sites and subsequently to the size of the TiO_2 nuclei and the radial growth-per-cycle (rGPC). We determined a maximum rGPC for TiO_2 of ~0.19 ± 0.02 nm at 60–120 °C and 0.15 ± 0.02 nm at 220 °C. A TiO_2 nucleus grows radially (while growing in volume) from a nucleation center, first covering the circumference of the SWCNT as it continues growing in the axial direction until meeting neighboring nuclei to coalesce. The radial growth of TiO_2 is mainly bound by the physisorption of TTIP molecules to the carbon surface once they are attached to the perimeter of the growing TiO_2 nuclei; and the eventual chemisorption of a TTIP molecule to a carbon atom occurs every ~12 nm (translating to a surface density of ~7000 μm^{-2}). Only 1% of the carbon atoms are chemically bonded to the TiO_2 film, keeping the majority of the carbon surface as sp^2. The reason why at higher temperatures (i.e. 220 °C) larger areas of uncoated nanotube surfaces are observed is because initially at these high temperatures one inevitably reduces the number of nucleation centers by "self-cleaning" and therefore increases the distance between them. This is also combined with a weaker adsorption of TTIP to the carbon surface leading to a lower rGPC. Quantifying the rGPC and thus the nuclei size of ALD coatings at any number of cycles allows determining the exact point of film closure in order to tailor the partial or complete surface coverage of quasi-inert substrate materials for a particular application.

CRediT authorship contribution statement

Carlos Guerra-Nuñez: Conceptualization, Methodology, Investigation, Formal analysis, Visualization, Writing - original draft, Writing - review & editing. **Barbara Putz:** Formal analysis, Visualization, Writing - review & editing, Funding acquisition. **Raluca Savu:** Resources. **Meng Li:** Resources, Investigation. **Yucheng Zhang:** Investigation, Resources. **Rolf Erni:** Supervision. **Stanislav Mochkalev:** Resources, Supervision. **Johann Michler:** Resources, Supervision. **Hyung Gyu Park:** Supervision. **Ivo Utke:** Conceptualization, Methodology, Project administration, Supervision, Writing - review & editing, Funding acquisition.

Declaration of Competing Interest

The authors declare that they have no known competing financial interests or personal relationships that could have appeared to influence the work reported in this paper.

Acknowledgments

We acknowledge the financial support of the SNF funding under the Sinergia project CRSII2_147615/1. We acknowledge a Seed Money Grant from the Leading House for the Latin American Region, Centro Latinoamericano-Suizo of the University of St. Gallen (CLS HSG) mandated by the Swiss State Secretariat for Education, Research and Innovation (SERI) under Grant Agreement No. SGM1728. B.P acknowledges funding from the EMPAPOSTDOCS-II program, which received funding from the European Union's Horizon 2020 research and innovation program under the Marie Skłodowska-Curie grant agreement number 754364.

Appendix A. Supplementary material

The frequency shifts of the RBM, D- and G Bands, the FWHM, the comparison between the I_D/I_G and A_D/A_G ratio, SEM images of 100 and 200 cycles of TiO2 deposited at 60, 120 and 220 °C. XPS measurements and comparison between I_D/I_G and sp^2/sp^3. The discussions and plots regarding the adaptation of the model from Lucchese and Cançado. Histograms of the diameter of the SWCNTs and TiO2 nuclei sizes for 100 cycles at 60 and 220 °C. All this information is supplied as supporting information.

Supplementary data to this article can be found online at https://doi.org/10.1016/j.apsusc.2021.149662.

References

[1] S. Eigler, Controlled Chemistry Approach to the Oxo-Functionalization of Graphene, Chemistry 22 (21) (2016) 7012–7027.
[2] Mariana Ioniță, George Mihail Vlăsceanu, Aiza Andreea Watzlawek, Stefan Ioan Voicu, et al., Graphene and functionalized graphene: Extraordinary prospects for nanobiocomposite materials, Compos. B Eng. 121 (2017) 34–57.
[3] J. Xu, Z. Cao, Y. Zhang, Z. Yuan, et al., A review of functionalized carbon nanotubes and graphene for heavy metal adsorption from water: Preparation, application, and mechanism, Chemosphere 195 (2018) 351–364.
[4] Michael F.L. De Volder, Sameh H. Tawfick, Ray H. Baughman, A. John Hart, Carbon Nanotubes: Present and Future Commercial Applications, Science 339 (6119) (2013) 535–539.
[5] Ray H. Baughman, Anvar A. Zakhidov, Walt A. de Heer, Carbon Nanotubes–the Route Toward Applications, Science 297 (5582) (2002) 787–792.
[6] L. Riikka, Puurunen, Surface chemistry of atomic layer deposition: A case study for the trimethylaluminum/water process, J. Appl. Phys. 97 (12) (2005), 121301.
[7] S.M. George, Atomic layer deposition: An overview, Chem. Rev. 110 (1) (2010) 111–131.
[8] H. Van Bui, F. Grillo, J.R. van Ommen, Atomic and molecular layer deposition: off the beaten track, Chem. Commun. (Camb.) (2016).
[9] Carlos Guerra-Nuñez, Max Döbeli, Johann Michler, Ivo Utke, Reaction and Growth Mechanisms in Al2O3 deposited via Atomic Layer Deposition: Elucidating the Hydrogen Source, Chem. Mater. 29 (20) (2017) 8690–8703.
[10] Catherine Marichy, Nicola Pinna, Carbon-nanostructures coated/decorated by atomic layer deposition: Growth and applications, Coord. Chem. Rev. 257 (23–24) (2013) 3232–3253.
[11] Catherine Marichy, Jean-Philippe Tessonnier, Marta C. Ferro, Kyeong-Hwan Lee, et al., Labeling and monitoring the distribution of anchoring sites on functionalized CNTs by atomic layer deposition, J. Mater. Chem. 22 (15) (2012) 7323.
[12] M. Burghard, Electronic and vibrational properties of chemically modified single-wall carbon nanotubes, Surf. Sci. Rep. (2005).
[13] N. Muhamad, A.B. Sulong, J. Sahari, R. Ramli, B. Deros, J. Park, Electrical Conductivity Behaviour of Chemical Functionalized MWCNTs Epoxy Nanocomposites, Eur. J. Sci. Res. 29 (1) (2009) 13–21.
[14] C. Guerra-Nunez, Y. Zhang, M. Li, V. Chawla, et al., Morphology and crystallinity control of ultrathin TiO layers deposited on carbon nanotubes by temperature-step atomic layer deposition, Nanoscale (2015).
[15] Yucheng Zhang, Carlos Guerra-Nuñez, Ivo Utke, Johann Michler, et al., Understanding and Controlling Nucleation and Growth of TiO2Deposited on Multiwalled Carbon Nanotubes by Atomic Layer Deposition, J. Phys. Chem. C (2015), 150203103227001.
[16] Yucheng Zhang, Carlos Guerra-Nunez, Meng Li, Johann Michler, et al., High Conformity and Large Domain Monocrystalline Anatase on MWCNT Core-shell Nanostructure: Synthesis, Structure and Interface, Chem. Mater. (2016).
[17] Yucheng Zhang, Carlos Guerra-Nuñez, Ivo Utke, Johann Michler, et al., Atomic Layer Deposition of Titanium Oxide on Single-Layer Graphene: An Atomic-Scale Study toward Understanding Nucleation and Growth, Chem. Mater. 29 (5) (2017) 2232–2238.
[18] Renato Cunha, Ricardo Paupitz, Kichul Yoon, C.T. Adri, Van Duin et al., Raman spectroscopy revealing noble gas adsorption on single-walled carbon nanotube bundles, Carbon 127 (2018) 312–319.
[19] W.T. van den Beld, M. Odijk, R.H. Vervuurt, J.W. Weber, et al., In-situ Raman spectroscopy to elucidate the influence of adsorption in graphene electrochemistry, Sci. Rep. 7 (2017) 45080.
[20] George Chimowa, Boitumelo Matsoso, Neil J. Coville, Suprakas Sinha Ray, et al., Preferential adsorption of NH3 gas molecules on MWCNT defect sites probed using in situ Raman spectroscopy, Physica Status Solidi (a) 214 (10) (2017) 1600930.
[21] Suresh C. Sharma, Dharmbir Singh, Ying Li, Raman scattering study of adsorption/desorption of water from single-walled carbon nanotubes, J. Raman Spectrosc. 36 (8) (2005) 755–761.
[22] R.A. Hackler, M.O. McAnally, G.C. Schatz, P.C. Stair, et al., Identification of Dimeric Methylalumina Surface Species during Atomic Layer Deposition Using Operando Surface-Enhanced Raman Spectroscopy, J. Am. Chem. Soc. 139 (6) (2017) 2456–2463.
[23] A. Merenda, Ed Ligneris, K. Sears, T. Chaffraix, et al., Assessing the temporal stability of surface functional groups introduced by plasma treatments on the outer shells of carbon nanotubes, Sci. Rep. 6 (2016) 31565.
[24] P. Vecera, S. Eigler, M. Kolesnik-Gray, V. Krstic, et al., Degree of functionalisation dependence of individual Raman intensities in covalent graphene derivatives, Sci. Rep. 7 (2017) 45165.
[25] P. Vecera, J.C. Chacon-Torres, T. Pichler, S. Reich, et al., Precise determination of graphene functionalization by in situ Raman spectroscopy, Nat. Commun. 8 (2017) 15192.
[26] R. Graupner, Raman spectroscopy of covalently functionalized single-wall carbon nanotubes, J. Raman Spectrosc. 38 (6) (2007) 673–683.
[27] F. Hof, S. Bosch, S. Eigler, F. Hauke, et al., New basic insight into reductive functionalization sequences of single walled carbon nanotubes (SWCNTs), J. Am. Chem. Soc. 135 (49) (2013) 18385–18395.
[28] George Bepete, Alain Pénicaud, Carlos Drummond, Eric Anglaret, Raman Signatures of Single Layer Graphene Dispersed in Degassed Water, "'Eau de Graphene"', J. Phys. Chem. C 120 (49) (2016) 28204–28214.
[29] G. Bepete, E. Anglaret, L. Ortolani, V. Morandi, et al., Surfactant-free single-layer graphene in water, Nat. Chem. 9 (4) (2017) 347–352.
[30] Luiz Gustavo Cançado, Mateus Gomes da Silva, Erlon H. Martins, Ferdinand Hof Ferreira, et al., Disentangling contributions of point and line defects in the Raman spectra of graphene-related materials, 2D Materials 4 (2) (2017).
[31] L.G. Cancado, A. Jorio, E.H. Ferreira, F. Stavale, et al., Quantifying defects in graphene via Raman spectroscopy at different excitation energies, Nano Lett. 11 (8) (2011) 3190–3196.
[32] R. Beams, L. Gustavo Cancado, L. Novotny, Raman characterization of defects and dopants in graphene, J. Phys. Condens. Matter 27 (8) (2015), 083002.
[33] E.H. Martins Ferreira, V.O. Marcus, F. Moutinho, M.M. Stavale, Lucchese et al., Evolution of the Raman spectra from single-, few-, and many-layer graphene with increasing disorder, Phys. Rev. B 82 (12) (2010).
[34] M.M. Lucchese, F. Stavale, E.H. Martins Ferreira, C. Vilani, et al., Quantifying ion-induced defects and Raman relaxation length in graphene, Carbon 48 (5) (2010) 1592–1597.
[35] J.H. Zhong, J. Zhang, X. Jin, J.Y. Liu, et al., Quantitative correlation between defect density and heterogeneous electron transfer rate of single layer graphene, J. Am. Chem. Soc. 136 (47) (2014) 16609–16617.
[36] A. Zandiatashbar, G.H. Lee, S.J. An, S. Lee, et al., Effect of defects on the intrinsic strength and stiffness of graphene, Nat. Commun. 5 (2014) 3186.
[37] Chia-Chi Chang, Chun-Chung Chen, I. Wei-Hsuan Hung, Kai Hsu et al., Strain-induced D band observed in carbon nanotubes, Nano Res. 5 (12) (2012) 854–862.
[38] Z. Liu, J. Zhang, B. Gao, Raman spectroscopy of strained single-walled carbon nanotubes, Chem Commun (Camb) 45 (2009) 6902–6918.
[39] Elena del Corro, Jesús González, Mercedes Taravillo, Emmanuel Flahaut, et al., Raman Spectra of Double-Wall Carbon Nanotubes under Extreme Uniaxial Stress, Nano Lett. 8 (8) (2008) 2215–2218.
[40] E. del Corro, M. Taravillo, J. González, V.G. Baonza, Raman characterization of carbon materials under non-hydrostatic conditions, Carbon 49 (3) (2011) 973–979.
[41] S. Osswald, E. Flahaut, Y. Gogotsi, In Situ Raman Spectroscopy Study of Oxidation of Double- and Single-Wall Carbon Nanotubes, Chem. Mater. 18 (6) (2006) 1525–1533.
[42] S. Osswald, E. Flahaut, H. Ye, Y. Gogotsi, Elimination of D-band in Raman spectra of double-wall carbon nanotubes by oxidation, Chem. Phys. Lett. 402 (4–6) (2005) 422–427.
[43] J. Donna, Nelson, Heather Rhoads, and Christopher Brammer, Characterizing Covalently Sidewall-Functionalized SWNTs, J. Phys. Chem. C 111 (48) (2007) 17872–17878.
[44] S.A. Chernyak, A.S. Ivanov, K.I. Maslakov, A.V. Egorov, et al., Oxidation, defunctionalization and catalyst life cycle of carbon nanotubes: a Raman spectroscopy view, Phys. Chem. Chem. Phys. 19 (3) (2017) 2276–2285.
[45] Shahir Hussain, Khurshed A. Shah, S.S. Islam, Investigation of effects produced by chemical functionalization in single-walled and multi-walled carbon nanotubes using Raman spectroscopy, Materials Science-Poland 31 (2) (2013) 276–280.
[46] Hiroki Komurasaki, Takahiro Tsukamoto, Kenji Yamazaki, Toshio Ogino, Layered Structures of Interfacial Water and Their Effects on Raman Spectra in Graphene-on-Sapphire Systems, J. Phys. Chem. C 116 (18) (2012) 10084–10089.
[47] René H.J. Vervuurt, Wilhelmus M.M. Erwin Kessels, Ageeth A. Bol, Atomic Layer Deposition for Graphene Device Integration, Adv. Mater. Interfaces 4 (18) (2017) 1700232.
[48] R.H. Vervuurt, B. Karasulu, M.A. Verheijen, W.E. Kessels, et al., Uniform Atomic Layer Deposition of Al2O3 on Graphene by Reversible Hydrogen Plasma Functionalization, Chem. Mater. 29 (5) (2017) 2090–2100.
[49] A. Moya, N. Kemnade, M.R. Osorio, A. Cherevan, et al., Large area photoelectrodes based on hybrids of CNT fibres and ALD-grown TiO2, J. Mater. Chem. A 5 (47) (2017) 24695–24706.
[50] A. Merlen, N. Bendiab, P. Toulemonde, A. Aouizerat, et al., Resonant Raman spectroscopy of single-wall carbon nanotubes under pressure, Phys. Rev. B 72 (3) (2005).
[51] J. Sandler, M.S.P. Shaffer, A.H. Windle, M.P. Halsall, et al., Variations in the Raman peak shift as a function of hydrostatic pressure for various carbon nanostructures: A simple geometric effect, Phys. Rev. B 67 (3) (2003).
[52] C. Thomsen, S. Reich, H. Jantoljak, I. Loa, et al., Raman spectroscopy on single- and multi-walled nanotubes under high pressure, Appl. Phys. A 69 (3) (1999) 309–312.
[53] Y.W. Sun, I. Hernández, A.J. Ghandour, C. Rice, et al., Resonance Raman spectroscopy of carbon nanotubes: pressure effects on G-mode, High Pressure Res. 34 (2) (2014) 191–197.
[54] Shohei Chiashi, Yoichi Murakami, Yuhei Miyauchi, Shigeo Maruyama, Temperature Dependence of Raman Scattering from Single-Walled Carbon

Nanotubes: Undefined Radial Breathing Mode Peaks at High Temperatures, Jpn. J. Appl. Phys. 47 (4) (2008) 2010–2015.
[55] Yingying Zhang, Liming Xie, Jin Zhang, Wu. Zhongyun, et al., Temperature Coefficients of Raman Frequency of Individual Single-Walled Carbon Nanotubes, J. Phys. Chem. C 111 (38) (2007) 14031–14034.
[56] N. Yang, M. Li, J. Patscheider, S.K. Youn, et al., A Forest of Sub-1.5-nm-wide Single-Walled Carbon Nanotubes over an Engineered Alumina Support, Sci. Rep. 7 (2017) 46725.
[57] R. Savu, J.V. Silveira, A. Flacker, A.R. Vaz, et al., Micro-reactors for characterization of nanostructure-based sensors, Rev. Sci. Instrum. 83 (5) (2012), 055104.
[58] W. Szmyt, C. Guerra, I. Utke, Diffusion of dilute gas in arrays of randomly distributed, vertically aligned, high-aspect-ratio cylinders, Beilstein J. Nanotechnol. 8 (2017) 64–73.
[59] Janne-Petteri Niemelä, Giovanni Marin, Maarit Karppinen, Titanium dioxide thin films by atomic layer deposition: a review, Semicond. Sci. Technol. (2017).
[60] M.S. Dresselhaus, G. Dresselhaus, R. Saito, A. Jorio, Raman spectroscopy of carbon nanotubes, Phys. Rep. 409 (2) (2005) 47–99.
[61] A.M. Rao, E. Richter, Shunji Bandow, Bruce Chase, et al., Diameter-Selective Raman Scattering from Vibrational Modes in Carbon Nanotubes, Science 275 (5297) (1997) 187–191.
[62] Reetu Kumari, Fouran Singh, Brajesh S. Yadav, Ravinder K. Kotnala, et al., Ion irradiation-induced, localized sp 2 to sp 3 hybridized carbon transformation in walls of multiwalled carbon nanotubes, Nucl. Instrum. Methods Phys. Res., Sect. B 412 (2017) 115–122.
[63] V.W. Brar, Ge G. Samsonidze, M.S. Dresselhaus, G. Dresselhaus, et al., Second-order harmonic and combination modes in graphite, single-wall carbon nanotube bundles, and isolated single-wall carbon nanotubes, Phys. Rev. B 66 (15) (2002).
[64] Elena del Corro, Miriam Peña-Álvarez, Michal Mračko, Radek Kolman, et al., Graphene under direct compression: Stress effects and interlayer coupling, Phys. Status Solidi (b) 253 (12) (2016) 2336–2341.
[65] M.J. Peters, L.E. McNeil, Jian Ping Lu, Daniel Kahn, Structural phase transition in carbon nanotube bundles under pressure, Phys. Rev. B 61 (9) (2000) 5939–5944.
[66] D. Christofilos, J. Arvanitidis, C. Tzampazis, K. Papagelis, et al., Raman study of metallic carbon nanotubes at elevated pressure, Diamond Relat. Mater. 15 (4–8) (2006) 1075–1079.
[67] X. Yu, Y. Shen, T. Liu, T.T. Wu, et al., Photocurrent generation in lateral graphene p-n junction created by electron-beam irradiation, Sci. Rep. 5 (2015) 12014.
[68] Matteo Bruna, Anna K. Ott, Mari Ijäs, Duhee Yoon, et al., Doping Dependence of the Raman Spectrum of Defected Graphene, ACS Nano 8 (7) (2014) 7432–7441.
[69] Rosanna Larciprete, Paolo Lacovig, Sandra Gardonio, Alessandro Baraldi, et al., Atomic Oxygen on Graphite: Chemical Characterization and Thermal Reduction, J. Phys. Chem. C 116 (18) (2012) 9900–9908.
[70] R. Timm, A.R. Head, S. Yngman, J.V. Knutsson, et al., Self-cleaning and surface chemical reactions during hafnium dioxide atomic layer deposition on indium arsenide, Nat. Commun. 9 (1) (2018) 1412.
[71] Sylwia Klejna, Simon D. Elliott, First-Principles Modeling of the “Clean-Up” of Native Oxides during Atomic Layer Deposition onto III–V Substrates, J. Phys. Chem. C 116 (1) (2012) 643–654.
[72] Jan M. Englert, Philipp Vecera, Kathrin C. Knirsch, Ricarda A. Schäfer, et al., Scanning-Raman-Microscopy for the Statistical Analysis of Covalently Functionalized Graphene, ACS Nano 7 (6) (2013) 5472–5482.
[73] Carlos Guerra-Nuñez, Max Döebeli, Johann Michler, Ivo Utke, Reaction and Growth Mechanisms in Al2O3 deposited via Atomic Layer Deposition: Elucidating the Hydrogen Source, Chem. Mater. (2017).
[74] J.C. Slater, Atomic Radii in Crystals, J. Chem. Phys. 41 (10) (1964) 3199–3204.
[75] H.B. Lee, S.H. Baeck, T.F. Jaramillo, S.F. Bent, Growth of Pt nanowires by atomic layer deposition on highly ordered pyrolytic graphite, Nano Lett. 13 (2) (2013) 457–463.